This is the Pre-Published Version.

The following publication Zhu, Z., To, S., Zhu, W.-L., Li, Y., & Huang, P. (2018). Optimum Design of a Piezo-Actuated Triaxial Compliant Mechanism for Nanocutting. IEEE Transactions on Industrial Electronics, 65(8), 6362–6371 is available at https://doi.org/10.1109/TIE.2017.2787592.

Optimum design of a piezo-actuated tri-axial compliant mechanism for nano-cutting

Zhiwei Zhu, *Member, IEEE*, Suet To, *Member, IEEE*, Wu-Le Zhu, *Member, IEEE*, Yangmin Li, *Senior Member, IEEE*, and Peng Huang

***Abstract*—A novel piezo-actuated compliant mechanism is developed to obtain tri-axial translational motions with decoupled features for nano-cutting. Analytical modeling of the working performance followed by Pareto-based multi-objective optimization is conducted for determining dimensions of the mechanism. Finite element analysis on the designed mechanism verifies the accuracy of the developed model, accordingly demonstrating the effectiveness of the optimal design process. Open-loop test on the prototype shows that proper strokes with low coupling and high natural frequencies are obtained as estimated. Low tracking error in closed-loop test suggests that the developed mechanism can precisely follow the desired trajectory to form complicated nanostructures. Finally, closed-loop based nano-sculpturing is conducted, demonstrating the effectiveness of the developed tri-axial motion system for nano-cutting well.**

***Index Terms*—Compliant mechanism, Piezoelectric actuator, Tri-axial translational motion, Multi-objective optimization, Nano-cutting.**

I. Introduction

Fast tool servo (FTS) assisted diamond cutting is widely regarded as an effective technique for the generation of freeform and micro/nanostructured surfaces with sub-micron form accuracy and nanometric surface roughness. Regarding the limited number of servo motions in the state-of-the-art FTS, the bi-axial and tri-axial oscillation based diamond cutting was recently introduced for enhancing the capability of generating more complicated micro/nanostructures. According to surface generation mechanism, the multi-axial oscillation based nano-cutting techniques which utilize a diamond tool to remove workpiece materials in the nanoscale can be categorized into surface nano-texturing [1]–[3] and nano-sculpturing [4]–[6]. With respect to nano-texturing, the diamond tool is vibrated under certain specified modes to form special micro/nanostructured textures. Meanwhile, as for nano-sculpturing, the diamond tool is actuated to follow an elliptical trajectory for material removal, and an especially designed motion component is simultaneously superimposed on the elliptical trajectory to form desired complicated shapes in nanoscale. In general, the resonant ultrasonic and non-resonant vibrations are adopted to construct the cutting motions used for both the two surface generation mechanisms. Although the resonant ultrasonic vibration based cutting has much higher efficiency [1], [6], [7], the non-resonant vibration provides much higher flexibility for the generation of more complicated micro/nanostructures [2], [8].

With the multi-axial non-resonant vibration based cutting, piezo-actuated multi-axial compliant mechanisms with parallel configuration are predominantly adopted to achieve high working frequency as well as high stiffness [4], [8], [9]. With nano-sculpturing, motions generated by the state-of-the-art compliant mechanisms were strongly coupled due to the coupled nature of the designed mechanism. The coupling induced motion inaccuracy may lead to deteriorated form accuracy of the generated structure. Although coupling effect as well as the inherent nonlinearity was fully investigated in nanopositioning stages [10], [11], very limited attention is paid to comprehensively compensate for these undesired effects in nano-sculpturing [8], [12]. Meanwhile, even the surface nano-texturing is dominated by using bi-axial ultrasonic elliptical vibration assisted cutting, the tri-axial non-resonant vibration is currently demonstrated to be more promising for the efficient generation of extremely complicated micro/nanostructures [2].

To realize non-resonant tri-axial translational motions for diamond cutting, Wada et.al proposed a three-axis controlled FTS for the sculpturing of both freeform and microstructured surfaces [13]. For the design of this device, three PEAs were orthogonally arranged and directly connected to the end-effector, forming the cubic configuration. Both the input and output ends of the mechanism were coupled without constraining undesired parasitic motions. Another tri-axial system for nano-sculpturing was developed by Gozen et. al [12], for which, the diamond tip was directly attached to a tri-axial PEA without using flexural structures for motion guidance. It is relatively simple, but suffers from limited motion range, low stiffness for stable cutting, and mutually coupled motions.

Manuscript received June 30, 2017; revised Month Sep 30, Nov 22, 2017; accepted Dec 14, 2017.

This work was jointly supported by the National Natural Science Foundation of China (51705254, 51675455), the Natural Science Foundation of Jiangsu Province (BK20170836), and the Fundamental Research Funds for the Central Universities (30917011301, 309171A8804).

Zhiwei Zhu is with School of Mechanical Engineering, Nanjing University of Science and Technology, Nanjing, J.S. 210094, China (e-mail: zw.zhu@njust.edu.cn).

Suet To is with the State Key Laboratory of Ultra-precision Machining Technology, Department of Industrial and Systems Engineering, The Hong Kong Polytechnic University, Kowloon, Hong Kong SAR, China (Corresponding author, phone: 852-27666587; fax: 852-23625267; e-mail: sandy.to@polyu.edu.hk).

Wu-Le Zhu is with the Department of Micro-Engineering, Kyoto University, Nishikyo-ku, Kyoto, 615-8540, Japan (e-mail: wule5033@gmail.com).

Yangmin Li is with Department of Industrial and Systems Engineering, The Hong Kong Polytechnic University, Kowloon, Hong Kong SAR, China (e-mail: yangmin.li@polyu.edu.hk).

Peng Huang is with College of Mechatronics and Control Engineering, Shenzhen University, Shenzhen, G.D. 518060, China (e-mail: huangp@szu.edu.cn).

By introducing a special set of "L"-shaped flexure hinges, Zhu et. al introduced a rotary tri-axial mechanism for nano-texturing [2], which is of compact dimensions, high working frequency, and decoupled outputs. However, the input ends of the mechanism were still coupled without proper isolation of PEAs, and the undesired rotational degree-of-freedom was not completely constrained in this design [9].

Recently, several kinds of tri-axial compliant mechanisms are developed for nano-manipulating, which are competitive candidates for implementing nano-cutting. With these mechanisms, cubic configuration is the most predominant to achieve tri-axial motions [14], [15], and motion decoupling was widely regarded as the most essential factor to guarantee motion accuracy and feedback control stability [15]–[17]. With current state-of-the-art decoupled mechanisms, a large number of compliant linkages are deliberately designed to isolate input motions, which may lead to low response speed induced by large moving inertia, as well as over-sized dimensions [15], [18], [19]. In addition, the complex mechanical structure may impose critical challenge for monolithic fabrication, and the commonly adopted assembly strategy can induce undesired misalignment error and over-large motion loss in the flexural connections [14], [15]. Moreover, over-usage of complicated linkages for motion isolation may lower the output stiffness of the mechanism to great extend, thereby limiting the applications to low-payloads and smooth working processes [19]. As discussed above, although the current designs have various good features, there are a wide spectrum of aspects to be improved, especially for the implementation of high efficient nano-cutting.

Regarding requirements for high compactness, high natural frequency, and high output stiffness, a novel monolithic compliant mechanism is proposed to deliver tri-axial translational motions for nano-cutting. With the mechanical design, effort needs to be devoted to analytically relating system stiffness as well as dynamics to structure dimensions, so as to provide basis for structure optimization. With performance modeling, the finite element theory based method is promising, but limited to the description of planar mechanisms [20], [21]. The inverse kinematic model (IKM) is capable of processing spatial mechanisms with complete compliance modeling, however, the assembled system matrix is relatively large especially for mechanisms with complicated mechanical structures and various moving bodies [22]–[24]. Although the matrix based compliance model (MCM) is concise for describing elastic deformation at a specified point, it loses detailed information about the induced deformations at other points in the mechanism [9], [16], [25].

To simplify the modeling process while maintain enough valuable information, a hybrid model combining the IKM and MCM is introduced for the description of the designed mechanism, and the Lagrangian method is then adopted to obtain the dynamics feature. After that, multiple design objectives are identified and optimized through the Pareto-based multi-objective optimization algorithm. Compared with the commonly adopted optimal design of compliant mechanisms, which converts the multiple objectives to be a single one [3], [15], [16], [23], [26], the adopted Pareto-based optimum is more objective, and provides more potential solutions for the design [27]. Based on the optimization, finite element analysis (FEA) is firstly adopted for its verification, and a prototype is accordingly fabricated and tested to investigate both open-loop and closed-loop performances of the mechanism. Finally, it is comprehensively demonstrated through conducting preliminary closed-loop based nano-sculpturing.

II. Mechanical Design of The Tri-axial Mechanism

The cubic structure is basically adopted to generate the tri-axial translational motions by arranging three identical uni-directional actuation mechanisms in a mutually orthogonal configuration. The three dimensional (3-D) mechanical structure of the developed compliant mechanism is illustrated in Fig. 1 (a). With motion along each direction, the popular double parallelogram mechanism (DPM) with eight right circular flexure hinges (RCFH) is adopted to isolate and to guide motion of the PEA. The generated motion is then transferred to the end-effector through a spatial transition mechanism (STM) consisting of four sets of parallelogram limbs as illustrated in Fig. 1 (b). With the limb, connection to the input and output ends is constructed through two bi-axial RCFHs with axially collocated notches [28], and an enlarged view of that is shown in Fig. 1 (c).

Without loss of generality, taking the uni-directional actuation along the x-axial direction for example, the limbs with bi-axial RCFH allows the end-effector to move along the y- and z-axial directions, while to maintain the primary motion along the x-axial direction. Taking advantage of the cuboid structure of the STM in Fig. 1 (b), the rotational motion of the end-effector around the y- and z-axes are constrained well. Based on the screw theory, motion of the end-effector is the intersection of allowable motions of the tri-axial identical actuation mechanisms [15], [29]. Thereby, the output motion of the mechanism can be determined by

$$\{x, y, z, \theta_x\}_1 \cap \{x, y, z, \theta_y\}_2 \cap \{x, y, z, \theta_z\}_3 = \{x, y, z\} \tag{1}$$

It is noteworthy that the actuation axes of the three actuation mechanisms are deliberately designed to intersect at one point to avoid undesired internal moments, thereby to eliminate potential parasitic motions induced by the moments. Furthermore, as discussed in [15], decoupled motion along each primary actuation direction can be achieved without inducing cross-talks along the other two translational directions, attributing to the orthogonal nature of the two rotational axes of the bi-axial RCFH, namely the 1^{-st} and 2^{-nd} axis in Fig. 1 (c). Therefore, a tri-axial translational mechanism with decoupled motions is obtained.

III. Mechanical Modeling of The Tri-axial Mechanism

To simplify the modeling process, we decompose the tri-axial mechanism into several compliant modules, mainly including the DPM and STM. Each of the module is modeled by the MCM method to obtain the basic elastic deformation

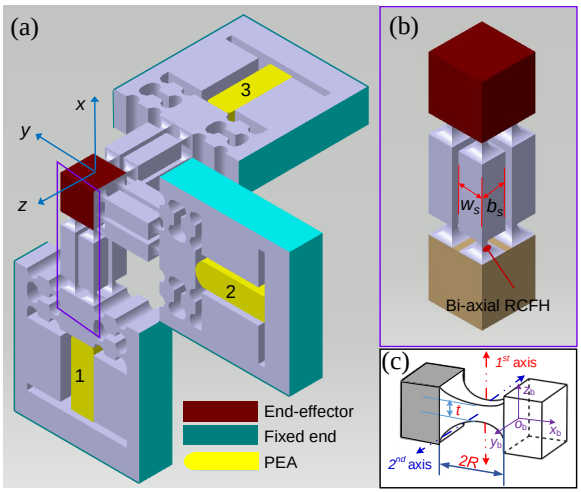

Fig. 1. Mechanical structure of the piezo-actuated mechanism, (a) 3-D model of the compliant mechanism, (b) the limbs for bi-axial motion guidance, and (c) the bi-axial RCFH with collocated notches.

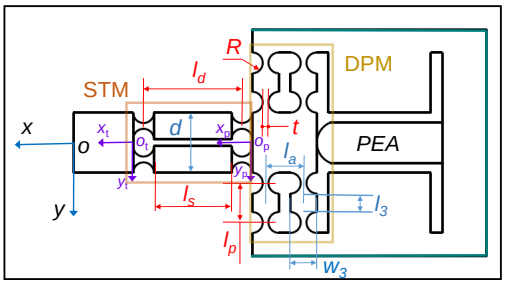

Fig. 2. Schematic of the actuation mechanism with labeled dimensions.

features, and the overall mechanism is accordingly modeled through the IKM method to obtain displacements at points needing attention, when subjected to external loads at any specified points.

A. Stiffness modeling of the actuation mechanism

Since the three actuation mechanisms are identical, only one is modeled in detail to avoid repetition. The actuation mechanism mainly consists of one DPM and one STM, and the dimensions are labeled as shown in Fig. 2.

1) Stiffness modeling of the DPM: As for the DPM, it mainly consists of four parallel linkages with symmetric structure, and each of the linkage is serially constructed through two RCFHs and one rectangular leaf-spring flexure hinge (LSFH). The complete compliance developed in Ref. [30] and the improved one adopted in Ref. [31] are employed for RCFHs and LSFHs, respectively.

Assume that the complete compliances of RCFHs and LSFHs are denoted by $\mathbf{C}_{\mathrm{R}}(R,t,b)$ and $\mathbf{C}_{\mathrm{L}}(L,w,b)$, where L, w, and b are the length, width, and thickness of the beam, the compliance of one linkage can be expressed in the local coordinate system $o_{\mathrm{p}}-x_{\mathrm{p}}y_{\mathrm{p}}z_{\mathrm{p}}$ by

$$\mathbf{C}_{\mathrm{p1}}=\sum_{i=1}^{2}\left(\mathbf{T}_i\mathbf{C}_{\mathrm{R}}\mathbf{T}_i^{\mathrm{T}}\right)+\mathbf{T}_3\mathbf{C}_{\mathrm{L}}\left(l_3,w_3,b\right)\mathbf{T}_3^{\mathrm{T}} \tag{2}$$

where $l_3=l_{\mathrm{p}}-2R$, $w_3=2R+t$, and $\mathbf{T}_i$ is the compliance transformation matrix (CTM) to transfer the local coordinate system of the hinges to the specified coordinate system. One can find detailed definition of the CTM in Ref. [16], [31].

Similar to that obtained in Eq. (2), the compliance of the second linkage can be obtained in the $o_{\mathrm{p}}-x_{\mathrm{p}}y_{\mathrm{p}}z_{\mathrm{p}}$ system as $\mathbf{C}_{\mathrm{p2}}$. Since the two linkages are connected to the platform in parallel, and the DPM is symmetric with respect to the $o_{\mathrm{p}}x_{\mathrm{p}}$ axis, stiffness of the DPM with respect to the point o_{p} can be obtained as

$$\mathbf{K}_{\mathrm{p}}=\left(\mathbf{C}_{\mathrm{p}}^{(\mathrm{L})}\right)^{-1}+\left[\mathbf{T}_{\mathrm{y}}\left(\pi\right)\mathbf{C}_{\mathrm{p}}^{(\mathrm{L})}\mathbf{T}_{\mathrm{y}}\left(\pi\right)^{\mathrm{T}}\right]^{-1} \tag{3}$$

with

$$\mathbf{C}_{\mathrm{p}}^{(\mathrm{L})}=\left[\left(\mathbf{C}_{\mathrm{p1}}\right)^{-1}+\left(\mathbf{C}_{\mathrm{p2}}\right)^{-1}\right]^{-1} \tag{4}$$

where $\mathbf{T}_{\mathrm{y}}\left(\pi\right)$ denotes the CTM conducting rotation operation around the $o_{\mathrm{p}}y_{\mathrm{p}}$ axis with an angular of π.

2) Stiffness modeling of the STM: With the STM, it mainly consists of four parallel limbs, with each serially connected by two bi-axial RCFH and one square beam. As for the bi-axial RCFH, the varying profiles along the two axes needs laborious integration operation for modeling its compliance by adopting the commonly used minimum energy method [28]. To avoid tedious integration, a finite beam based matrix modeling is introduced by evenly dividing the bi-axial RCFH along the $o_{\mathrm{p}}x_{\mathrm{p}}$ axis into N elements [31]. Therefore, the width (thickness) of the cross-section of the k-th element in its local system $o_{\mathrm{p}}-x_{\mathrm{p}}y_{\mathrm{p}}z_{\mathrm{p}}$ can be expressed by

$$w(k)=b(k)=t+2R-\sqrt{\frac{4kR^2}{N}-\left(\frac{2kR}{N}\right)^2} \tag{5}$$

Since the bi-axial RCFH can be regarded as a serial connection of the N elements, its compliance in the $o_{\mathrm{p}}-x_{\mathrm{p}}y_{\mathrm{p}}z_{\mathrm{p}}$ system can be obtained as

$$\mathbf{C}_{\mathrm{b}}=\sum_{k=1}^{N}\left[\mathbf{T}_k^{(\mathrm{b})}\mathbf{C}_{\mathrm{L}}\left(\frac{2R}{N},w(k),b(k)\right)\left(\mathbf{T}_k^{(\mathrm{b})}\right)^{\mathrm{T}}\right] \tag{6}$$

where $\mathbf{T}_k^{(\mathrm{b})}$ represents the CTM from the local system of the k-th square beam to the $o_{\mathrm{p}}-x_{\mathrm{p}}y_{\mathrm{p}}z_{\mathrm{p}}$ system.

With the limb, the length and width (thickness) for the beam connecting the two bi-axial RCFHs are $l_{\mathrm{s}}=l_{\mathrm{d}}-2R$, $w_{\mathrm{s}}=b_{\mathrm{s}}=2R+t$. Considering the serial nature, the compliance of the limb can be obtained in the local system $o_{\mathrm{t}}-x_{\mathrm{t}}y_{\mathrm{t}}z_{\mathrm{t}}$ of the STM as

$$\mathbf{C}_{\mathrm{t1}}=\sum_{i=1}^{2}\left[\mathbf{T}_i^{\mathrm{t}}\mathbf{C}_{\mathrm{b}}\left(\mathbf{T}_i^{\mathrm{t}}\right)^{\mathrm{T}}\right]+\mathbf{T}_3^{\mathrm{t}}\mathbf{C}_{\mathrm{L}}\left(l_{\mathrm{s}},w_{\mathrm{s}},b_{\mathrm{s}}\right)\left(\mathbf{T}_3^{\mathrm{t}}\right)^{\mathrm{T}} \tag{7}$$

where $\mathbf{T}_i^{\mathrm{t}},\ i=1,2,3$ is the CTM from the local system of the i-th hinge to the $o_{\mathrm{t}}-x_{\mathrm{t}}y_{\mathrm{t}}z_{\mathrm{t}}$ system.

Similarly, the compliance of the second limb can be obtained as $\mathbf{C}_{\mathrm{t2}}$ Since the four limbs are rotationally symmetric around the $o_{\mathrm{t}}x_{\mathrm{t}}$ axis, the stiffness of the STM at the o_{t} point can be expressed in the $o_{\mathrm{t}}-x_{\mathrm{t}}y_{\mathrm{t}}z_{\mathrm{t}}$ system as

$$\mathbf{K}_{\mathrm{s}}=\mathbf{C}_{\mathrm{tu}}^{-1}+\left[\mathbf{T}_{\mathrm{x}}\left(\pi\right)\mathbf{C}_{\mathrm{tu}}\mathbf{T}_{\mathrm{x}}\left(\pi\right)^{\mathrm{T}}\right]^{-1} \tag{8}$$

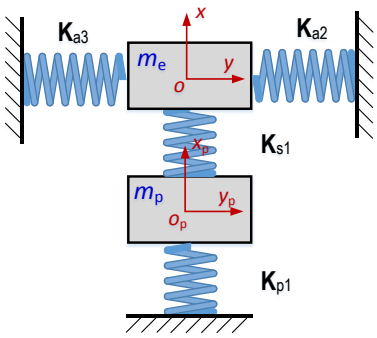

Fig. 3. The equivalent spring-mass system of the tri-axial compliant mechanism, where $\mathbf{K}_{a2}$ and $\mathbf{K}_{a3}$ are the stiffness matrices of the other two actuation mechanisms expressed in the $o-xyz$ system, respectively; $\mathbf{K}_{p1}$ and $\mathbf{K}_{s1}$ are stiffness matrices of the DPM and STM in the $o-xyz$ system in the x-axial actuation mechanism, respectively; m_p and m_e are the equivalent mass of the intermediate platform in the DPM and the end-effector, respectively.

with

$$\mathbf{C}_{tu}=\left[(\mathbf{C}_{t1})^{-1}+(\mathbf{C}_{t2})^{-1}\right]^{-1} \tag{9}$$

where $\mathbf{T}_x(\pi)$ denotes the CTM adopting operation around the $o_t x_t$ axis with an angular of π.

3) Stiffness modeling of the actuation mechanism: As illustrated in Fig. 2, the DPM and STM are serially connected with respect to the end-effector. Therefore, the stiffness of the actuation mechanism at point o can be expressed in the $o-xyz$ system by

$$\mathbf{K}_a=\left[\mathbf{T}_{po}(\mathbf{K}_p)^{-1}\mathbf{T}_{po}^{T}+\mathbf{T}_{to}(\mathbf{K}_s)^{-1}\mathbf{T}_{to}^{T}\right]^{-1} \tag{10}$$

where $\mathbf{T}_{po}$ and $\mathbf{T}_{to}$ are the CTMs from the $o_p-x_p y_p z_p$ and $o_t-x_t y_t z_t$ systems to the $o-xyz$ system, respectively.

B. Inverse kinematics model of the compliant mechanism

Without considering mechanical properties of PEAs, the tri-axial compliant mechanism can be equivalent as the spring-mass system as illustrated in Fig. 3. Based on the Hooke's law, the governing equation for the elastic deformation of the mechanism can be expressed by

$$\begin{bmatrix}\mathbf{K}_{ee} & \mathbf{K}_{ep}\\ \mathbf{K}_{pe} & \mathbf{K}_{pp}\end{bmatrix}\begin{bmatrix}\mathbf{u}_e\\ \mathbf{u}_p\end{bmatrix}=\begin{bmatrix}\mathbf{F}_e\\ \mathbf{F}_p\end{bmatrix} \tag{11}$$

where $\mathbf{u}_e=[u_{ex},u_{ey},u_{ez},\theta_{ex},\theta_{ey},\theta_{ez}]^T$ and $\mathbf{u}_p=[u_{px},u_{py},u_{pz},\theta_{px},\theta_{py},\theta_{pz}]^T$ are the displacement vectors of the end-effector and the intermediate platform in the DPM, respectively; and $\mathbf{F}_e=[f_{ex},f_{ey},f_{ez},M_{ex},M_{ey},M_{ez}]^T$ and $\mathbf{F}_p=[f_{px},f_{py},f_{pz},M_{px},M_{py},M_{pz}]^T$ are the corresponding external loads.

$$\begin{aligned}\mathbf{K}_{ee}=&\mathbf{K}_{a2}+\mathbf{K}_{a3}+\mathbf{K}_{s1}\\ =&\sum_{j=1}^{2}\left[\mathbf{T}_{ai}(\mathbf{K}_a)^{(-1)}\mathbf{T}_{ai}^{T}\right]^{(-1)}+\mathbf{K}_{s1}\end{aligned} \tag{12}$$

$$\begin{aligned}\mathbf{K}_{pp}=&\mathbf{K}_{p1}+\mathbf{K}_{s1}\\ =&\left[\mathbf{T}_p(\mathbf{K}_p)^{(-1)}\mathbf{T}_p^{T}\right]^{(-1)}+\mathbf{K}_{s1}\end{aligned} \tag{13}$$

$$\mathbf{K}_{ep}=\mathbf{K}_{pe}=-\mathbf{K}_{s1}=-\left[\mathbf{T}_s(\mathbf{K}_s)^{(-1)}\mathbf{T}_s^{T}\right]^{(-1)} \tag{14}$$

where $\mathbf{T}_{ai}$, $\mathbf{T}_p$ and $\mathbf{T}_s$ are the CTMs from the local coordinate systems of the two actuation mechanisms, the DPM, and the CTM to the global system $o-xyz$, respectively.

The output stiffness of the tri-axial mechanism is defined as the required directional force at the output point o to generate unit displacement at the same point. By setting $\mathbf{F}_p=\mathbf{O}$, and $\mathbf{u}_e=[1,0,0,0,0,0]$, the required force $\hat{\mathbf{F}}_e$ can be obtained by solving Eq. (11) as

$$\hat{\mathbf{F}}_e=\left(\mathbf{K}_{ee}-\mathbf{K}_{s1}\mathbf{K}_{pp}^{-1}\mathbf{K}_{s1}\right)\mathbf{u}_e \tag{15}$$

Therefore, the output stiffness along the ox axis can be obtained as $k_{out}=\hat{\mathbf{F}}_e(1)$.

Similarly, the input stiffness can be defined as the required force along the actuation direction at the input point o_p to generate unit displacement at the same point. By setting $\mathbf{F}_e=\mathbf{O}$, and $\mathbf{u}_p=[1,0,0,0,0,0]$, the required force $\hat{\mathbf{F}}_p$ can be obtained by solving Eq. (11) as

$$\hat{\mathbf{F}}_p=\left(\mathbf{K}_{pp}-\mathbf{K}_{s1}\mathbf{K}_{ee}^{-1}\mathbf{K}_{s1}\right)\mathbf{u}_p \tag{16}$$

The input stiffness along the actuation axis can be obtained as $k_{in}=\hat{\mathbf{F}}_p(1)$.

When subjected to the actuation force $\mathbf{F}_p=[F_{PEA},0,0,0,0,0]$ generated by the PEA and the external load $\mathbf{F}_e$, the corresponding output displacement of the end-effector $\mathbf{u}_e$ can be expressed by

$$\mathbf{u}_e=\left(\mathbf{K}_{ee}-\mathbf{K}_{s1}\mathbf{K}_{pp}^{-1}\mathbf{K}_{s1}\right)^{-1}\left(\mathbf{F}_e+\mathbf{K}_{s1}\mathbf{K}_{pp}^{-1}\mathbf{F}_p\right) \tag{17}$$

Meanwhile, the displacement of the intermediate platform $\mathbf{u}_p$ in the DPM can be accordingly expressed by

$$\begin{aligned}\mathbf{u}_p=&\mathbf{K}_{s1}^{-1}\left(\mathbf{K}_{ee}-\mathbf{F}_e\right)\\ =&\left(\mathbf{K}_{pp}-\mathbf{K}_{s1}\mathbf{K}_{ee}^{-1}\mathbf{K}_{s1}\right)^{-1}\left(\mathbf{F}_e+\mathbf{K}_{s1}\mathbf{K}_{ee}^{-1}\mathbf{F}_e\right)\end{aligned} \tag{18}$$

In general, the output displacement of the end-effector $\mathbf{u}_e(1)$ along the actuation direction will decrease due to the elastic deformation of the connected flexure hinges. Let χ represent the displacement loss, which is defined by $\chi=1-\mathbf{u}_e(1)/\mathbf{u}_p(1)$, the maximum output displacement of the mechanism along one direction can be expressed by

$$d_1=\frac{k_{pea}}{k_{pea}+k_{in}}(1-\chi)\,d_{pea} \tag{19}$$

where d_{pea} and k_{pea} denote the nominal displacement and stiffness of the employed PEA, respectively.

C. Dynamic model of the tri-axial mechanism

Since the mechanism is identical with respect to each direction, only the natural frequency with deformation along one direction is modeled. Assume that a displacement of u is generated at the input end along the actuation direction, the induced output of the end-effector is $u_e=(1-\chi)u$. Therefore, the equivalent lumped motion of the limb for the corresponding STM can be estimated to be $u_s=0.5(u+u_e)$. Therefore, the kinematic energy of the mechanism can be expressed by

$$U=\frac{m_p\dot{u}^2}{2}+2m_s\dot{u}_s^2+\frac{m_e\dot{u}_e^2}{2}+\frac{J_p}{2}\left(\frac{\dot{u}}{l_p}\right)^2+4J_s\left(\frac{\dot{u}_e}{l_d}\right)^2 \tag{20}$$

where $J_{\rm p}$ and $J_{\rm s}$ are the rotary inertia of the connection linkages and limbs in the DPM and STM, respectively. The last term in Eq. (20) is rotational kinetic energy of the other two STMs induced by the primary motion u.

Based on the Lagrangian principle, the natural frequency can be obtained as

$$f = \frac{1}{2\pi}\sqrt{\frac{k_{\rm in}}{M}} = \frac{1}{2\pi}\sqrt{k_{\rm in}\left(\frac{1}{\ddot{u}}\frac{\partial U}{\partial u}\right)^{-1}} \tag{21}$$

where M is the equivalent moving mass of the mechanism.

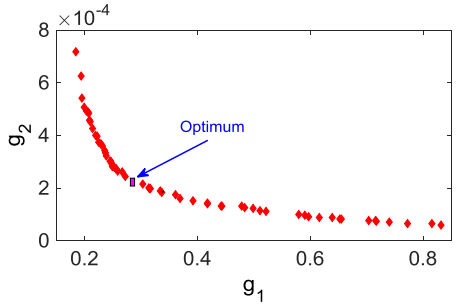

Fig. 4. The obtained Pareto optimum front.

IV. Multi-objective Optimal Design of The Tri-axial Mechanism

A. Problem Statement

Overall, the working performance of the tri-axial mechanism is highly sensitive to structure dimensions, especially the ones governing the shapes of the flexure hinges and the relative positions between the hinges [9], [32]. With the actuation mechanism, the symmetry of the STM suggests that the thickness and width of both the end-effector and the intermediate platform in the DPM will equal to each other, as marked by d in Fig. 2. Since the relative distance between limbs in the STM has very limited influence on its performance [26], it will be directly set as $d = 4R+2t+1.2\ mm$. Similarly, the relative distance between the two linkages in the DPM is set as $l_{\rm a} = 2R+t+2\ mm$, and accordingly, the length of the intermediate platform is $l_{\rm m} = l_{\rm a} + 2R + t$. Therefore, there are only four independent parameters that govern the working performance of the mechanism, namely, R, t, $l_{\rm p}$ and $l_{\rm d}$.

As for nano-cutting, the following requirements are of the utmost importance:

1) High natural frequency f to achieve high working bandwidth, and accordingly high machining efficiency;
2) Large stroke d_1 with low displacement loss χ to guarantee enough output displacement as well as high actuation efficiency;
3) High output stiffness $k_{\rm out}$ to guarantee machining accuracy and stability;
4) Low equivalent von Mises stress in the mechanism when subjecting to maximum input. In this study, this criterion will be checked through FEA model after selecting proper dimensional parameters;
5) Large fatigue safety factor to guarantee fatigue reliability. Considering structure complexity and multi-axial loading condition, it will also be checked through FEA model after selecting dimensional parameters.

In general, the two conflicting requirements, namely the natural frequency f and the stroke d_1, need to be deliberately balanced. With the output stiffness $k_{\rm out}$, it may vary but has no conflict with the input stiffness. Regarding this essential relationship, the optimal design can be stated as follows:

1) Objective function: maximize the natural frequency and the stroke as well. To have a high output stiffness $k_{\rm out}$, it is optimized to be close to the input stiffness $k_{\rm in}$. Mathematically, it takes the form as

$$\min \begin{cases} g_1 = \dfrac{1}{1-\chi}\cdot\dfrac{k_{\rm in}}{k_{\rm in}+k_{\rm pea}} + \left|1-\dfrac{k_{\rm out}}{k_{\rm in}}\right| \\ g_2 = f^{-1} \end{cases} \tag{22}$$

2) Optimization variables: $\mathbf{P} = [R, t, l_{\rm p}, l_{\rm d}]$.
3) Subject to: Parameter ranges are set by considering both the machinability and structure compactness, and they are set as: $\mathbf{P}_{\min} \in [1.5, 0.5, 1, 5]$ mm and $\mathbf{P}_{\max} \in [5, 1, 10, 15]$ mm.

As discussed above, it is a multi-objective optimization problem with multiple variables and strong nonlinearity. To solve this problem, a Pareto-based multi-objective differential evolution algorithm is adopted, and one can refer to Ref. [33] for more details about the algorithm.

B. Optimization Results and FEA Investigation

The selected material for the mechanism is spring steel with elasticity modulus of 206 GPa, passion ratio of 0.28, and mass density of 7850 $\rm kg/m^3$. The nominal stroke and stiffness of the PEA are $d_0 = 15\ \mu$m and $k_{\rm pea} = 100\ \rm N\cdot\mu m^{-1}$, respectively. By conducting the multi-objective optimization, the obtained Pareto optimum front is illustrated in Fig. 4. To make a balance between the two objectives g_1 and g_2, an solution at the labeled point in Fig. 4 where performance variation turns to be relatively flat is chosen as the optimum. The corresponding optimal dimensions are $\hat{\mathbf{P}} = [1.8, 1, 6.8, 13.5]$ mm, which lead to the mechanism with $k_{\rm in} = 20.19\ \rm N\cdot\mu m^{-1}$, $k_{\rm out} = 18.41\ \rm N\cdot\mu m^{-1}$, and $f = 3875$ Hz. Considering the stiffness of the PEA, the maximum input displacement will be $d_{\rm in} = 12.48\ \mu$m.

To verify the analytical model, FEA through the Workbench module in ANSYS software is conducted, and the 3D tetrahedron element with proximity and curvature based size function is adopted to mesh the model. Applying a surface force of $F_{\rm x} = 100$ N along the x-axis leads to a directional deformation at the input end of about 5.336 μm, suggesting an input stiffness of about $k_{\rm in} = 18.74\ \rm N\cdot\mu m^{-1}$. Similarly, the output stiffness is also assessed by applying the x-axial force at the output end, which is about $k_{\rm out} = 16.93\ \rm N\cdot\mu m^{-1}$. The comparison between the analytical and FEA results are summarized in Table I. Taking FEA results as the benchmark, both the relative errors of the input and output stiffness are

TABLE I
SUMMARY OF THE ANALYTICAL AND FEA RESULTS.

k_{in} / N $\cdot$ μm^{-1}			k_{out} / N $\cdot$ μm^{-1}			f / Hz		
Anal.	FEA	Err.	Anal.	FEA	Err.	Anal.	FEA	Err.
20.19	18.74	7.74%	18.41	16.93	8.74%	3875	3473	11.6%

less than 10%, demonstrating the accuracy and reliability of the developed analytical model for structure optimization.

When subjected to the maximum input displacement d_{in} along the three directions, the equivalent stress distribution obtained by FEA shows that the maximum stress occurs at the outer surface of the mid-point of the RCFH in each DPM, which is of about 104.4 MPa. It is far below the yield stress of the selected steel (520-690 MPa), showing that repeatable elastic deformation can be obtained during working. To investigate the fatigue behavior, Gerber based mean stress theory using the maximum principle stress is adopted to derive the safety factor through ANSYS/Workbench based FEA simulation [34]. With full consideration of stress concentration and surface roughness effects, a conservation fatigue strength factor is set as 0.85, and the default material fatigue parameters for steel in the software are employed for the analysis. To mimic the working process, three harmonic motions ranging from zero to the maximum displacement d_{in} are simultaneously applied at the three input ends, leading to a minimum safety factor of about $S_{\text{f}} = 1.34 > 1$ at the aforementioned point with maximum static equivalent stress. It suggests that reliability against fatigue failure can be guaranteed well for the designed mechanism.

Modal analysis through FEA is further conducted to investigate dynamic features of the mechanism. The first three resonant modes occur with desired translational deformations along the three directions, and the natural frequencies are about 3472.7 Hz, 3481.6 Hz and 3484.1 Hz. Although the mechanism is symmetric, the discrepancy between the resonant frequencies for the three modes may attribute to the mesh difference and calculation errors. Regarding the FEA results, the relative error of the natural frequency obtained by analytical model is about 11.6% as summarized in Table I, which is induced by the overestimation of input stiffness in the analytical model.

Moreover, it is noteworthy that when the maximum displacement $d_{\text{in}} = 12.48$ μm is applied along the x-axis, both the resulted displacements at the input ends of the y- and z-axial actuation mechanisms are about 35.6 nm. Meanwhile, the induced lateral outputs of the end-effector along the y- and z-axial directions are about 6 nm and 8 nm, respectively. Regarding the neglectable parasitic motions at both the input and output ends, the tri-axial mechanism is decoupled well to implement independent motion along each direction.

V. PROTOTYPE PERFORMANCE TESTING

To have a comprehensive investigation on practical performances of the optimized tri-axial mechanism, an off-line experimental testing system is constructed. During the testing, the power PMAC control board (Delta Tau Data Systems, USA) with eight input-output channels is employed to generate and gather signals of the three axial motions in both open-loop and closed-loop tests. The command signals generated by the control board are then amplified by three power amplifiers (PI E617.001, Germany) to drive the three orthogonal PEAs (PI P-887.51, Germany). The resulted displacement of the tri-axial mechanism is then measured by a precision capacitive displacement sensing system (Elite, Lion Precision, USA) with five channels. The captured displacements are then gathered by the control board for further analysis or feedback control. The experimental setup is graphically illustrated in Fig. 5.

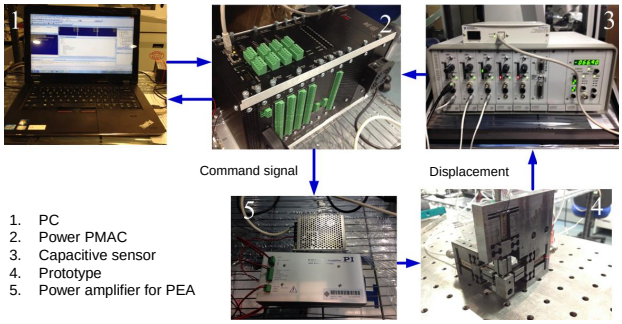

Fig. 5. Experimental setup for performance testing.

A. Open-loop Testing

To assess the practical stroke along each direction, harmonic command signal with low frequency of 1 Hz and full-span voltage of 10 V is applied to each actuator separately, resulting in the responses shown in Fig. 6. The obtained strokes are about 12.37 μm, 13.14 μm and 11.72 μm along the x-, y- and z-axial directions, respectively. In general, all of them are very close to the theoretical value of about 12.48 μm. From the parasitic motions shown in Fig. 6, the primary motion along the x-axial direction induces the maximum parasitic motion along the z-axial direction (about 3.8%). When actuated along the y- and z-axial directions, the induced parasitic motions along the other two directions are consistent, which are about 1.37% and 2.51% of the corresponding actuation motions.

In principle, the designed mechanism is free from parasitic motions as investigated through FEA in section IV-B, and the average coupling ratio of about 2.56% in tests might be caused by manufacturing errors or misalignment of the actuation axes. Compared with the average ratios of the state-of-the-art mechanisms as reported in [15], [35], and [13] which are about 3.59%, 7.8%, and 10%, respectively, the designed mechanism demonstrates to have a superior decoupling property. The low-level parasitic motions may allow the implementation of single-input-single-output (SISO) controller for feedback control of the three axes.

To characterize frequency response of the mechatronic system, a swept excitation using voltage with amplitude of 1 V and frequency linearly ranging from 1 Hz to 5 kHz is employed to independently drive each PEA. The resulted frequency response functions along the three directions are illustrated in Fig. 7, which show almost consistent features with each other. The natural frequency for each direction

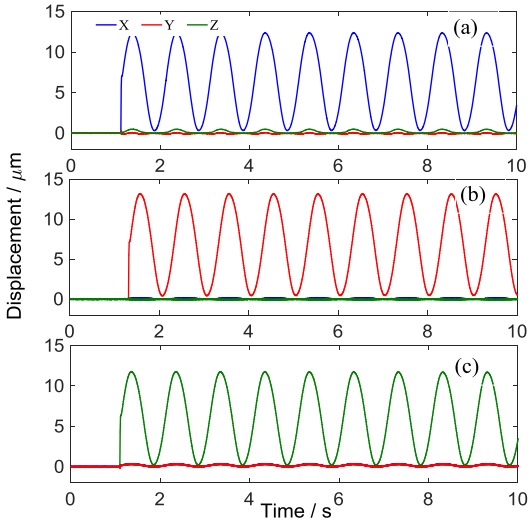

Fig. 6. Full span harmonic response and the corresponding coupling motions with independent actuation along, (a) the x-, (b) the y-, and (c) the z-axial direction.

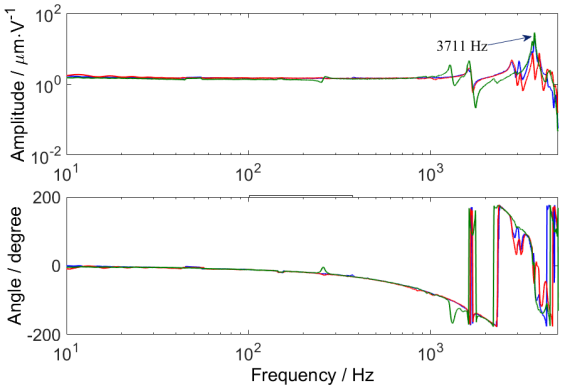

Fig. 7. Characteristics of the frequency responses of the mechanism along the three actuation directions.

is around 3.7 kHz. It is slightly higher than that obtained through FEA (around 3.5 kHz), attributing to the stiffness enhancement by adding PEAs in experimental testing. In addition, the amplitude-frequency response along each direction is relatively flat with frequency less than 1 kHz, suggesting that the mechanism can perform well within this frequency range.

It is noteworthy that the non-ideal constraint of the base of the mechanism may lead to undesired resonant vibrations of the base. This phenomenon is observed as small fluctuations in the amplitude-frequency response function with respect to frequency ranging from 200 Hz to 300 Hz and 1 kHz to 3.7 KHz. To avoid this and accordingly to have a much wider working frequency, special holder for proper constraint of the base of the mechanism needs to be specially considered in the near future.

B. Closed-loop Testing

As discussed above, the decoupling feature allows the usage of SISO controller for the mechanism to compensate for the inherent nonlinearity of PEAs as well as external load

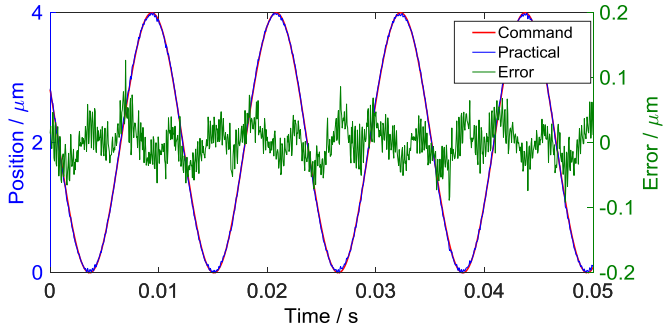

Fig. 8. Characteristics of the harmonic tracking performance.

disturbances. A typical Proportion-Integration-Differentiation (PID) controller is employed for the feedback control. Meanwhile, a low pass filter with cut-off frequency of 200 Hz is adopted to eliminate influences of system noises, and a velocity feedforwad compensator is also employed to enhance the response speed of the system. Parameters for the controller are determined through the trail-and-error method.

With nano-cutting, continuous harmonic-like motion will be the predominant trajectory for the mechanism to follow. To assess the trajectory tracking performance, harmonic signal with amplitude of 2 μm and frequency of 90 Hz is adopted as the desired motion. To avoid repetition, only the tracking performance along the x-axis direction is illustrated in Fig. 8, showing a tracking error of around $\pm$70 nm, which is about $\pm$1.75% of the motion span. When tracking a signal with higher frequency, the tracking error will increase, suggesting that more advanced control algorithm needs to be further developed in the future to improve the tracking performance, especially for high-frequency applications.

VI. Preliminary Nano-sculpturing Experiments

To demonstrate the effectiveness of the developed tri-axial motion system, preliminary nano-sculpturing experiment is conducted. For this process, the target is to generate surface with complicated shapes in the nano-scale, and the dimension accuracy is crucial for this process. Therefore, cutting is conducted in the closed-loop to precisely control the cutting motions.

A. Experimental setup

In this study, the nano-sculpturing experiment is implemented on an ultra-precision machine tool (Moore Nanotech 350FG, USA) for convenient rough cutting as well as alignment of the relative position between the tool and workpiece. Natural single crystal diamond tool (Contour Fine Tooling, U.K.) with sharp edge as illustrated in Fig. 10 is employed for material removal. The workpiece material is brass C2600. The diamond tool is fixed on the spindle as graphically presented in Fig. 9, and an enlarged view of the cutting space is further illustrated at the corner of this photo. During cutting, the spindle together with the sharp diamond tool is fixed as static, and the rake face of the tool is parallel with the $o_{\mathrm{m}} - x_{\mathrm{m}} z_{\mathrm{m}}$ plane. After cutting, the generated nanostructures

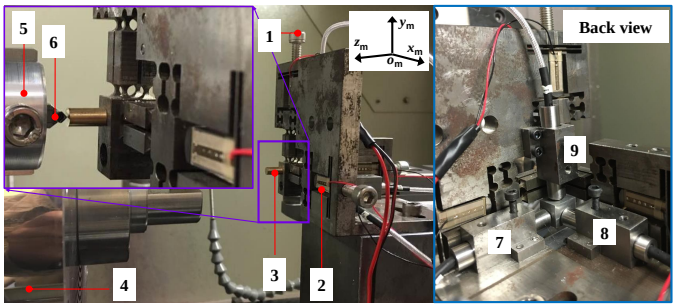

Fig. 9. Experimental setup for the nano-cutting, where $o_{\mathrm{m}}-x_{\mathrm{m}}y_{\mathrm{m}}z_{\mathrm{m}}$ is the coordinate system of the machine tool; 1. pre-loading screw for the PEA; 2. PEA; 3. workpiece; 4.spindle; 5. fixture for the tool; 6. diamond tool; 7, 8 and 9: three capacitive sensors.

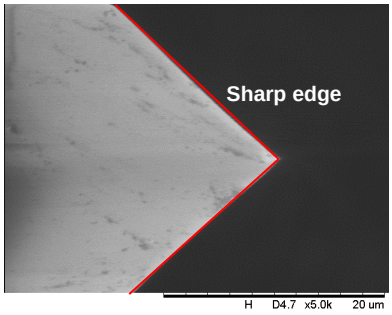

Fig. 10. SEM images of the used diamond tool with sharp edge.

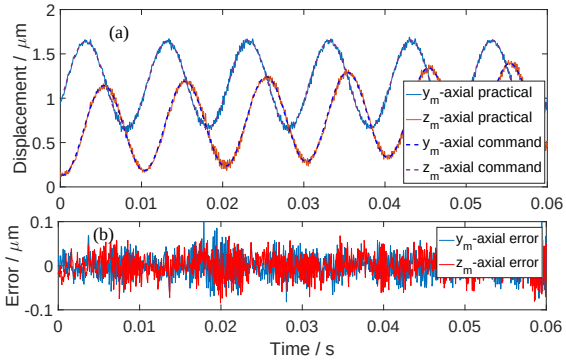

Fig. 11. Tracking performance of motions along the y_{m}- and z_{m}-axial directions, (a) the trajectory tracking, and (b) the tracking errors

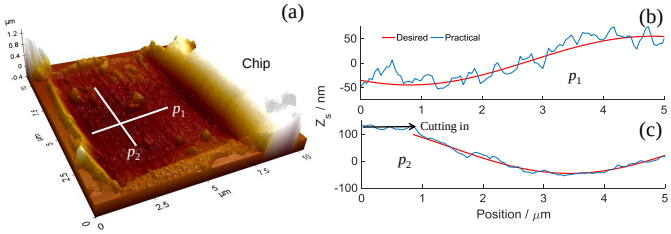

Fig. 12. Characteristics of the nano-sculptured sinusoidal grid surface, (a) the 3-D structure, (b) and (c) the cross-sectional profiles along the p_1 and p_2 directions, respectively.

are characterized through a atomic force microscopy (AFM, XE-70, Park Systems, Korean).

Primarily, harmonic motions with a amplitude of 0.5 μm as well as a consistent frequency of 90 Hz are adopted for the PEAs along both the y_{m}- and z_{m}-axial directions to construct the basic nano-fly-cutting motion for material removal. Meanwhile, a linear motion with constant velocity of 7.5 μm/s is concurrently implemented by the y_{m}-axial PEA to construct the forward feeding motion. Moreover, actuation of the x_{m}-axial PEA with a speed of 50 nm per step is also adopted as the lateral step feeding motion. Overall, the tri-axial motions forms the basic nano-cutting motion for material removal.

B. Results and discussion

A sinusoidal grid surface with $z_{\mathrm{s}} = A\sin\left(2\pi T_{\mathrm{x}}^{-1}x_{\mathrm{s}}\right) + A\cos\left(2\pi T_{\mathrm{y}}^{-1}y_{\mathrm{s}}\right)$ is fabricated, and the amplitude and spatial frequency of the surface are $A = 100$ nm and $T_{\mathrm{x}}^{-1} = T_{\mathrm{y}}^{-1} = 8$ μm. To form this curved nanostructure, a specified trajectory determined by the geometry of the desired surface is superimposed on the basic harmonic vibration along the z_{m}-axial direction. Since the x_{m}-axial position is fixed during cutting, only the performance of tacking fast motions along both the y_{m}- and z_{m}-axial directions is illustrated in Fig. 11 (a), and the tracking error is further shown in Fig. 11 (b), demonstrating relatively high tracking accuracy. It is noteworthy that the noise observed during cutting is slightly larger than that obtained in off-line tracking in Fig. 8, which might be caused by external disturbance induced from interactions between the tool and workpiece.

The resulted 3-D AFM image is shown in Fig. 12 (a), and the two cross-sectional profiles along the p_1 and p_2 directions as marked in Fig. 12 (a) are further illustrated respectively in Figs. 12 (b) and 12 (c). From the 3-D structure in Fig. 12 (a), the chip mainly flow along the side rather than the rake face direction of the tool, forming a big piece of chip without breaking to be at one side of the cutting region. In addition, small debris are observed on the machined surface. Profiles shown in Fig. 12 (b) and (c) shows much bigger fluctuation along the p_1 direction, which induced by the lateral step feeding motion. As for both the two profiles, good agreement between the practical and desired shapes are achieved.

It is noteworthy that with the sub-micron depth of-cut, the cutting force may range from about dozens of micronewtons to several millinewtons [36], [37]. Therefore, influences of cutting forces on the tool motion can be ignored with full consideration of the relatively high output stiffness of the mechanism. Another issue related to the structure generation might be the temperature increase induced by fast vibrations of the piezo-actuators, and thermal deformations of the mechanism may deteriorate the fabrication accuracy. In general, the thermal deformation is difficult to measure or compensate for during the nano-cutting process, and further efforts on it will be conducted in the future.

VII. Conclusion

In this paper, a novel piezoelectrically actuated compliant mechanism is developed to deliver tri-axial translational motions for nano-cutting. With the mechanism, three identical actuation mechanisms are orthogonally arranged to achieve

the tri-axial motion, and the cuboid structure using bi-axial flexure hinges is introduced for motion guidance, as well as for rotation constraint of the end-effector.

With the design, a hybrid analytical model is introduced to describe the elastic deformation behavior of the mechanism, and the Lagrangian method is employed for modeling system dynamics. Based on the formulated model, Pareto-based multi-objective optimization is accordingly conducted to optimally determine dimensions of the designed mechanism.

Performance of the optimized mechanism is theoretically verified through finite element analysis (FEA), and good agreement between the analytical and FEA results demonstrates the effectiveness of the design process well. A prototype is then fabricated and experimentally assessed in terms of practical stroke, de-coupling behavior, natural frequency, and trajectory tracking performance. Finally, preliminary closed-loop based nano-sculpturing further verifies the effectiveness of the developed system for nano-cutting.

REFERENCES

[1] P. Guo and K. F. Ehmann, "Development of a tertiary motion generator for elliptical vibration texturing," *Precision Engineering*, vol. 37, no. 2, pp. 364–371, 2013.

[2] Z. Zhu, S. To, K. F. Ehmann, G. Xiao, and W. Zhu, "A novel diamond micro-/nano-machining process for the generation of hierarchical micro-/nano-structures," *Journal of Micromechanics and Microengineering*, vol. 26, no. 3, p. 035009, 2016.

[3] W.-L. Zhu, Z. Zhu, Y. He, K. Ehmann, B. Ju, and S. Li, "Development of a novel 2d vibration-assisted compliant cutting system for surface texturing," *IEEE/ASME Transactions on Mechatronics*, vol. 22, no. 4, pp. 1796–1806, 2017.

[4] D. Brehl and T. Dow, "Review of vibration-assisted machining," *Precision engineering*, vol. 32, no. 3, pp. 153–172, 2008.

[5] B. A. Gozen and O. B. Ozdoganlar, "Design and evaluation of a mechanical nanomanufacturing system for nanomilling," *Precision Engineering*, vol. 36, no. 1, pp. 19–30, 2012.

[6] J. Zhang, T. Cui, C. Ge, Y. Sui, and H. Yang, "Review of micro/nano machining by utilizing elliptical vibration cutting," *International Journal of Machine Tools and Manufacture*, vol. 106, pp. 109–126, 2016.

[7] E. Shamoto, N. Suzuki, E. Tsuchiya, Y. Hori, H. Inagaki, and K. Yoshino, "Development of 3 dof ultrasonic vibration tool for elliptical vibration cutting of sculptured surfaces," *CIRP Annals-Manufacturing Technology*, vol. 54, no. 1, pp. 321–324, 2005.

[8] X. Zhou, C. Zuo, Q. Liu, and J. Lin, "Surface generation of freeform surfaces in diamond turning by applying double-frequency elliptical vibration cutting," *International Journal of Machine Tools and Manufacture*, vol. 104, pp. 45–57, 2016.

[9] Z. Zhu, S. To, K. F. Ehmann, and X. Zhou, "Design, analysis, and realization of a novel piezoelectrically actuated rotary spatial vibration system for micro-/nano-machining," *IEEE/ASME Transactions on Mechatronics*, vol. 22, no. 3, pp. 1227 – 1237, 2017.

[10] D. Habineza, M. Rakotondrabe, and Y. Le Gorrec, "Bouc–wen modeling and feedforward control of multivariable hysteresis in piezoelectric systems: application to a 3-dof piezotube scanner," *IEEE Transactions on Control Systems Technology*, vol. 23, no. 5, pp. 1797–1806, 2015.

[11] Z. Li and J. Shan, "Inverse compensation based synchronization control of the piezo-actuated fabry-perot spectrometer," *IEEE Transactions on Industrial Electronics*, DOI 10.1109/TIE.2017.2711511, 2017.

[12] B. A. Gozen and O. B. Ozdoganlar, "A method for open-loop control of dynamic motions of piezo-stack actuators," *Sensors and Actuators A: Physical*, vol. 184, pp. 160–172, 2012.

[13] T. Wada, M. Takahashi, T. Moriwaki, and K. Nakamoto, "Development of a three axis controlled fast tool servo for ultra precision machining (2nd report)- study of micro-groove machining by applying tool vibration cutting," *Journal of the Japan Society for Precision Engineering*, vol. 74, no. 5, pp. 486–490, 2008.

[14] J.-P. Bacher, S. Bottinelli, J.-M. Breguet, and R. Clavel, "Delta3: design and control of a flexure hinge mechanism," *Proc. SPIE*, vol. 4568, pp. 135–142, 2001.

[15] Y. Li and Q. Xu, "A totally decoupled piezo-driven xyz flexure parallel micropositioning stage for micro/nanomanipulation," *IEEE Transactions on Automation Science and Engineering*, vol. 8, no. 2, pp. 265–279, 2011.

[16] Y. Li and Q. Xu, "Design and analysis of a totally decoupled flexure-based xy parallel micromanipulator," *IEEE Transactions on Robotics*, vol. 25, no. 3, pp. 645–657, 2009.

[17] H. Tang and Y. Li, "Development and active disturbance rejection control of a compliant micro-/nanopositioning piezostage with dual mode," *IEEE Transactions on Industrial Electronics*, vol. 61, no. 3, pp. 1475–1492, 2014.

[18] X. Zhang and Q. Xu, "Design of a new flexure-based xyz parallel nanopositioning stage," in *Robotics and Biomimetics (ROBIO), 2015 IEEE International Conference on*, pp. 1962–1966. IEEE, 2015.

[19] G. Hao and H. Li, "Design of 3-legged xyz compliant parallel manipulators with minimised parasitic rotations," *Robotica*, vol. 33, no. 04, pp. 787–806, 2015.

[20] H. Wang and X. Zhang, "Input coupling analysis and optimal design of a 3-dof compliant micro-positioning stage," *Mechanism and Machine Theory*, vol. 43, no. 4, pp. 400–410, 2008.

[21] W.-L. Zhu, Z. Zhu, Y. Shi, X. Wang, K. Guan, and B.-F. Ju, "Design, modeling, analysis and testing of a novel piezo-actuated xy compliant mechanism for large workspace nano-positioning," *Smart Materials and Structures*, vol. 25, no. 11, p. 115033, 2016.

[22] J. W. Ryu, D.-G. Gweon, and K. S. Moon, "Optimal design of a flexure hinge based $xy\phi$ wafer stage," *Precision Engineering*, vol. 21, no. 1, pp. 18 – 28, 1997.

[23] L.-J. Lai, G.-Y. Gu, and L.-M. Zhu, "Design and control of a decoupled two degree of freedom translational parallel micro-positioning stage," *Review of Scientific Instruments*, vol. 83, no. 4, p. 045105, 2012.

[24] H. Kim, J. Kim, D. Ahn, and D. Gweon, "Development of a nano-precision 3-dof vertical positioning system with a flexure hinge," *IEEE Transactions on Nanotechnology*, vol. 12, no. 2, pp. 234–245, 2013.

[25] F. Wang, H. Zhang, C. Liang, Y. Tian, X. Zhao, and D. Zhang, "Design of high-frequency ultrasonic transducers with flexure decoupling flanges for thermosonic bonding," *IEEE Transactions on Industrial Electronics*, vol. 63, no. 4, pp. 2304–2312, 2016.

[26] Z. Zhu, X. Zhou, Q. Liu, and S. Zhao, "Multi-objective optimum design of fast tool servo based on improved differential evolution algorithm," *Journal of Mechanical Science and Technology*, vol. 25, no. 12, pp. 3141–3149, 2011.

[27] R. Wang and X. Zhang, "Parameters optimization and experiment of a planar parallel 3-dof nanopositioning system," *IEEE Transactions on Industrial Electronics*, DOI 10.1109/TIE.2017.2736502, 2017.

[28] N. Lobontiu and E. Garcia, "Two-axis flexure hinges with axially-collocated and symmetric notches," *Computers & Structures*, vol. 81, no. 13, pp. 1329–1341, 2003.

[29] J. Yu, S. Li, H.-j. Su, and M. Culpepper, "Screw theory based methodology for the deterministic type synthesis of flexure mechanisms," *ASME Journal of Mechanisms and Robotics*, vol. 3, no. 3, p. 031008, 2011.

[30] Y. Wu and Z. Zhou, "Design calculations for flexure hinges," *Review of Scientific Instruments*, vol. 73, no. 8, pp. 3101–3106, 2002.

[31] Z. Zhu, X. Zhou, R. Wang, and Q. Liu, "A simple compliance modeling method for flexure hinges," *Science China Technological Sciences*, vol. 58, no. 1, pp. 56–63, 2015.

[32] H. Huang, H. Zhao, Z. Ma, L. Hu, J. Yang, G. Shi, C. Ni, and Z. Pei, "Design and analysis of the precision-driven unit for nano-indentation and scratch test," *Journal of Manufacturing Systems*, vol. 31, no. 1, pp. 76–81, 2012.

[33] S. Das and P. N. Suganthan, "Differential evolution: A survey of the state-of-the-art," *IEEE transactions on Evolutionary Computation*, vol. 15, no. 1, pp. 4–31, 2011.

[34] F. Dirksen, M. Anselmann, T. I. Zohdi, and R. Lammering, "Incorporation of flexural hinge fatigue-life cycle criteria into the topological design of compliant small-scale devices," *Precision Engineering*, vol. 37, no. 3, pp. 531 – 541, 2013.

[35] S. Awtar, J. Ustick, and S. Sen, "An xyz parallel-kinematic flexure mechanism with geometrically decoupled degrees of freedom," *Journal of Mechanisms and Robotics*, vol. 5, no. 1, p. 015001, 2013.

[36] W. Gao, R. J. Hocken, J. A. Patten, and J. Lovingood, "Force measurement in a nanomachining instrument," *Review of scientific instruments*, vol. 71, no. 11, pp. 4325–4329, 2000.

[37] W. Gao, R. J. Hocken, J. A. Patten, J. Lovingood, and D. A. Lucca, "Construction and testing of a nanomachining instrument," *Precision Engineering*, vol. 24, no. 4, pp. 320–328, 2000.

Zhiwei Zhu (S'14-M'16) was born in Nantong, JS China. He received his B.E. & M.S. degrees in mechanical engineering from Jilin University, China, in 2010 and 2013, respectively; and Ph.D. degree in industrial and systems engineering from the Hong Kong Polytechnic University, HK SAR, China, in 2016.

He is currently a professor in School of Mechanical Engineering with Nanjing University of Science and Technology, Nanjing, JS China. From March 2016 to September 2016, he was a Post-Doctoral Research Fellow with the Hong Kong Polytechnic University, HK SAR, China. From October 2015 to January 2016, he was a Pre-Doctoral Research Fellow with Northwestern University, Evanston, IL USA. His research interests include ultraprecision machining of freeform optics, smart micro/nanomanufacturing, and design, modeling and control of precision mechatronic systems for measurement as well as manufacturing.

Suet To (M'17) obtained her MPhil in Material Science from Brunel University in the UK in 1993, and her PhD in Ultra-precision Machining Technology from The Hong Kong Polytechnic University, HK SAR, China, in 2000.

She is currently an Associate Professor of the Department of Industrial and Systems Engineering of The Hong Kong Polytechnic University and Associate Director of State Key Laboratory in Ultra-precision Machining Technology and Advanced Optics Manufacturing Centre. She is an active researcher who focuses on industry-related and applied research in Ultra-precision Machining; Advanced Optics Manufacturing; Precision Injection Moulding and Material Science. She has published more than 150 international journal papers and international conference papers in various fields of precision engineering, advanced optics manufacturing and material science. She has secured more than 10 external projects as Principal Investigator (PI)/Project Coordinator (PC) over the last a few years. She has successfully obtained a total amount of HK$20 millions research grants.

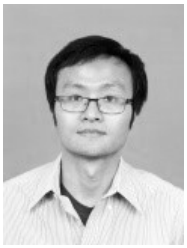

Wu-Le Zhu (M'16) received his B.E. degree in mechanical design manufacturing and its automation from Hefei University of Technology, China, in 2011; and Ph.D. degree in mechatronic engineering from Zhejiang University, Hangzhou, China, in 2016.

He is currently a Post-doctoral research fellow with the Department of Micro Engineering, Kyoto University, Japan. From 2014 to 2016, he was a visiting pre-doctoral research fellow with Northwestern University, USA. His research interests include design, modeling and control of mechatronic systems, ultraprecision diamond machining of freeform surfaces.

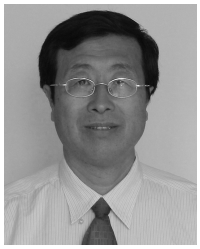

Yangmin Li (M'98-SM'04) received the B.S. and M.S. degrees from Jilin University, Changchun, China, in 1985 and 1988, respectively, and the Ph.D. degree from Tianjin University, Tianjin, China, in 1994, all in mechanical engineering.

He is currently a Full Professor of the Department of Industrial and Systems Engineering of The Hong Kong Polytechnic University. He has authored and coauthored 381 papers in journals, book chapters and conferences. His research interests include micro/nanomanipulation, compliant mechanism, precision engineering, robotics, multibody dynamics and control.

Prof. Li is currently an Associate Editor of the IEEE Trans. Auto. Sci. Eng., Associate Editor of Mechatronics, and Associate Editor of the International Journal of Control, Automation, and Systems. He is a Member of the ASME and CSME.

Peng Huang was born in Zunyi, GZ China. He received his B.E. degree in mechanical engineering from Hefei University of technology, Hefei, China, in 2009; M.S. degree in mechatronics engineering from Harbin Institute of Technology, Harbin, China, in 2011; and Ph.D. degree in industrial and systems engineering from the Hong Kong Polytechnic University, HK SAR, China, in 2016.

He is currently an assistant professor in College of Mechatronics and the Control Engineering of Shenzhen University. His research interests include error measurement and compensation of machine tools, spindle dynamics and machining of biomedical surfaces.